SEISMIC ANISOTROPY ANALYSIS IN THE VICTORIA LAND REGION (ANTARCTICA)

Salimbeni S. [1], Pondrelli S.[1], Danesi S.[1] , Morelli A. [1]

[1] *Istituto Nazionale di Geofisica e Vulcanologia, Sezione di Bologna, Via D. Creti 12, 40128 Bologna, Italy; salimbeni@bo.ingv.it*

ABSTRACT

We present shear-wave splitting results obtained from analysis of core refracted teleseismic phases recorded by permanent and temporary seismographic stations located in the Victoria Land region (Antarctica). We used eigenvalue technique to linearize the rotated and shifted shear-wave particle motion, in order to determine the best splitting parameters. A well-scattered distribution of single shear-wave measurements has been obtained. Average values show clearly that dominant fast axis direction is NE-SW oriented, accordingly with previous measurements obtained around this zone. Only two stations, OHG and STAR show different orientations, with N-S and NNW-SSE main directions. On the basis of the periodicity of single shear-wave splitting measurements with respect to back-azimuths of events under study, we inferred the presence of lateral and vertical changes in the deep anisotropy direction. To test this hypothesis we have modelling waveforms using a cross-convolution technique in one and two anisotropic layer's cases. We obtained a significant improvement on the misfit in the double layer case for the cited couple of stations. For stations where a multi-layer structure does not fit, we looked for evidences of lateral anisotropy changes at depth through Fresnel zone computation. As expected, we find that anisotropy beneath the Transantarctic Mountains (TAM) is considerably different from that beneath the Ross Sea. This feature influences the measurement distribution for the two permanent stations TNV and VNDA. Our results show a dominant NE-SW direction over the entire region, but other anisotropy directions are present and find an interpretation when examined in the context of regional tectonics.

INTRODUCTION

Teleseismic shear-wave splitting is a powerful tool to investigate the structure of the upper mantle in different geodynamic environments. Since anisotropy is in relation with deformational events, shear-wave splitting studies permit to understand and to review the geodynamical processes acted in the area of interest.

Shear-wave splitting is the seismological analogous to the optical birefringence. When an S-wave passes through an anisotropic medium, it will be split into two quasi-S waves travelling with different velocities [*Savage*, 1999]. The polarization direction of the faster phase and the difference in arrival time (delay time) between the two phases, are parameters recovered from this analysis. Teleseismic shear-wave splitting of core-refracted phases (e.g. SKS, SKKS) provides information about the anisotropy located on the station-side of the epicenter-station path. Most of the anisotropy contribution is originated in the upper mantle region where olivine is the most abundant mineral [*Savage*, 1999; *Silver*, 1996]. Since olivine is highly anisotropic, its crystals develop a preferred orientation when a geodynamical process acts. In the simple shear case, Lattice Preferred Orientation (LPO) is generated by dislocation glide [*Karato et al.*, 2008] and [100] crystallographic-axis rotates parallel to the direction of the maximum shear [*Savage*, 1999] that also corresponds to the faster direction of S-wave polarization after splitting. Therefore the study of anisotropy can provide information about deformational processes acted at a regional scale.

64 The harsh climatic conditions and the inaccessibility of the Antarctic region determine the
65 difficulty to activate permanent or long-term seismic instrumentation projects; few data are
66 actually available, therefore any information added to the acquired knowledge become very
67 important for an improved characterization of polar zones. In the last years several studies on
68 seismic anisotropy have been carried on.
69 In East Antarctica, previous shear-wave splitting studies for the Dronning Maud Land area
70 [*Bayer et al.*, 2007] suggested mainly NE-SW anisotropy direction, with some nearly N-S
71 directions, that authors interpreted as due to crust-mantle coupling deformation. NE-SW also
72 results the main direction for stations located in other inland areas (e.g., at South Pole; [*Muller*,
73 2001]), whereas shear-wave splitting measurements for coastal stations are generally oriented
74 parallel to the coast line such as on the Lambert Glacier region [*Reading and Heintz*, 2008]. In
75 West Antarctica, NE-SW continues to be the dominant direction beneath the Transantarctic
76 Mountain (TAM) belt [*Barklage et al.*, 2009] and in the Victoria Land region [*Pondrelli and*
77 *Azzara*, 1998; *Pondrelli et al.*, 2005]. These measurements are interpreted as generated by the
78 TAM uplift, while NW-SE and E-W directions, present sporadically around the Ross Sea, are
79 interpreted as linked to some extensional processes acted on the past.
80
81 Some studies found also indications of possible two-layer anisotropic structure. In the Lambert
82 Glacier and Wilkes Land areas, *Reading and Heintz* [2008] inferred the presence of a two-layer
83 structure for coastal stations, as due to a combination of pre-existing lineation added to the
84 present-day mantle flow; *Muller* [2001] instead proposed the presence of a two anisotropic layers
85 beneath the Scotia Plate and beneath the western stations of Dronning Maud Land. In this last

86 case, the anisotropy sampled on the upper layer would be the signature of an Archaean frozen-in
87 anisotropy while the origin of the lower layer would go back to the Gondwana rifting stages.
88
89 In the following, we describe the anisotropy measured for the Victoria Land region, Western
90 Antarctica. Using data recorded at both permanent and temporary Italian stations we show the
91 indications for the presence of different local domains of anisotropy, with a possible double-layer
92 anisotropic system with lateral changes, a configuration more complex than that previously
93 shown for this region.
94
95

GEOLOGICAL AND GEOPHYSICAL SETTINGS

Antarctica is commonly divided into two main geological domains, East and West, with very different structural and geophysical characteristics (Figure 1).

East Antarctica (EA) is classified as a Precambrian craton, the central part of the Palaeozoic Gondwana super-continent. Flat sedimentary rocks cover the granitic intrusion present in the area [*Tingey*, 1991].

West Antarctica (WA) is interpreted as the assembly of Meso-Cenozoic crustal blocks [*Dalziel and Elliot* 1982] or micro-plates with metamorphic and volcanic terranes [*Anderson*, 1999]. The Ross Sea and the West Antarctic Rift System (WARS) are part of West Antarctica and represent the extensional basins developed after Cretaceous and Cenozoic extensions [*Behrendt*, 1999]. Evidence of active alkaline volcanism is present with Mount Erebus and Mount Melbourne volcanoes (Figure 1).

The Transantarctic Mountains (TAM) separates Eastern from Western regions. The TAM is a 3500 Km long and 200 Km wide chain composed together with its eastern part (Victoria Land region) by Cambrian and younger rocks. The TAM is considered an intra-continental mountain belt with lack of evidence of compression. Its origin is attributed to an asymmetric uplift of the crust along the Ross embayment flank and subsequent denudation from Cretaceous to Cenozoic time [*Studinger et al.*, 2004]. Fission track analyses [*Fitzgerald*, 1992] establish the beginning of the main uplift phase at about 50 Ma.

116 The geological and geodynamical history of the Antarctic region is very complex but, limiting the
117 analysis to the Victoria Land region, most of the surface and deeper geological structures can be
118 ascribed to the Ross Orogeny. The Meso-Cenozoic evolution of the Ross Sea has seen two main
119 phases of extension - from 105 to 55 Ma characterized by E-SE extensional faulting and from 55
120 to 32 Ma generating N-S and NNW-SSE tectonic depression - and the last right-lateral strike-slip
121 tectonics from 32 Ma to the present.
122 Surface structures in the Victoria Land region can be divided into 3 principal fault systems
123 [*Salvini and Storti*, 1999]. The first is NW-SE right-hand strike-slip faulting along which the
124 major glaciers streams; the second is composed by N-S depressions interpreted as extensional or
125 transtensional structures associated to Cenozoic, right-lateral shear; the third includes NE-SW
126 and NNE-SSW faults present in the Terra Nova Bay area, bordering the western shoulder of the
127 Ross Sea which are connected to the TAM uplift. Faults are parallel to the coastline and tend to
128 rotate to N-S and NW-SE moving towards south.
129
130 The tectonic fabric of the crystalline basement also originated during the Ross Orogeny, but in
131 early Palaeozoic times (500-480 Ma). The fabric is defined by steeply dipping metamorphic
132 foliation, highly strained shear zones and fold axial trends, in a main NW-SE direction [*Salvini*
133 *and Storti*, 1999].
134
135 Seismological studies on several geophysical parameters also provide structural information,
136 which unsurprisingly keep trace of the dramatic discontinuity between East and West Antarctica.
137 Combining receiver function and phase velocity inversions, *Lawrence et al.* [2006b] derived

138 crustal thickness in various parts of the study region. They show that beneath the Ross Sea the
139 crust is 20 Km thick (+- 2 Km), and increases to 40 Km (+- 2 Km) beneath the TAM chain. A
140 uniform 35 Km thick crustal layer would characterize the cratonic domain in East Antarctica.
141 These values are also in agreement with several previous works [*Bannister et al.*, 2003; *Bentley*,
142 1991; *ten Brink et al.*, 1997]. The crustal structure of Northern Victoria Land has been
143 investigated also by *Piana Agostinetti et al.* [2004]. Analysing receiver functions they find a
144 crustal thickness of 24 Km in the Robertson Bay area, with an increase to 31 Km moving
145 westwards from the Transantarctic Mountain (Oates Land). This would suggest that the crustal
146 profile remains approximately stable moving southwards beneath coastal stations, while it
147 changes laterally (at different longitudes). Beneath the TAM chain the authors find evidence of
148 two Moho interfaces between 26 and 48 Km.

149 Another seismological difference between East and West Antarctica concerns shear-wave
150 velocities. The TAM divides a “fast” Eastern upper mantle with velocities of 4.5 Km/s (typical of
151 a continental shield) from a ”slower” Western one where velocities decrease to 4.2 Km/s (typical
152 for active tectonics and volcanic regions). These values are in agreements also with those inferred
153 from the study of regional surface wave velocities [*Danesi and Morelli*, 2001; *Morelli and*
154 *Danesi*, 2004; *Ritzwoller et al.*, 2001]. The transition occurs at 100 (+- 50) Km inland near the
155 crest of the TAM [*Lawrence et al.*, 2006c]. The same transition separates a colder Eastern region
156 from a warmer Western one [*Lawrence et al.*, 2006a]. The increment in mantle temperature is
157 200-400 °C (at 80-220 Km depth) corresponding to a reduction of 1% in density.

158

159 Previous shear-wave splitting measurements in Victoria Land region and neighbouring areas are
160 shown in Figure 2. *Pondrelli et al.* [2005] measured shear-wave splitting in the Northern part of
161 the study area (in purple in Figure 2). Only non-null splitting measurements are plotted in the
162 map, at location corresponding to piercing points at 150 Km of depth. Near TNV station,
163 measurements have NE-SW dominant fast velocity direction while only few data have a different
164 pattern. The average delay time is 1.6 s. The authors linked this NE-SW direction to the presence
165 of an old cratonic anisotropy and to mantle flows due to the growth of the TAM chain. The other
166 directions (E-W and NW-SE) instead are interpreted as due to the extensional processes
167 associated with the Western Rift system.

168

169 Results from the TAMSEIS Project (in yellow in Figure 2) are taken from *Barklage et al.* [2009].
170 They obtained shear-wave splitting teleseismic measurements for 3 temporary arrays (yellow
171 triangles) located principally on the southern part of the Victoria Land and extending inland
172 toward East Antarctica. Splitting parameters are calculated using stacked-waveforms; at the
173 intersections between E-W and N-S array the anisotropy is N58E and become more E-W moving
174 towards the coast (N67E). The delay time is about 1 sec. At the same intersection, comparing
175 Rayleigh wave phase velocities from different azimuth, *Lawrence et al.* [2006c] found a fast axis
176 direction from 55° to 85° with magnitude of 1.5-3.0% of anisotropy. In this area, *Barklage et al.*
177 [2009] suggest anisotropy associated with an upper mantle flow related to Cenozoic Ross Sea
178 extension or an edge-driven convection due to the sharp thermal change between West and East
179 Antarctica. Towards the East Antarctica instead the measurements are uniformly distributed with
180 a N60E (+- 10°) direction but show a rotation of 15°-20° (becoming E-W) in two highlands parts

(Belgica and Vostock). The main distribution is described as due to a relict tectonic fabric while the E-W measurements are interpreted as due to different extensional events maybe associated with older tectonic process.

STATIONS AND DATA

We used data recorded by 11 seismic stations belonging to permanent and temporary networks in the Victoria Land region (Figure 2 and Table S1 on auxiliary material).

Permanent stations (cyan triangles in Figure 2) TNV and VNDA are located respectively on the northern and southern margins of the study region. Both stations are equipped with 3-component broadband sensors (Streckeisen STS-1 and Geoteck KS-54000 Borehole respectively) with free access data availability managed by IRIS consortium.

In the region also temporary stations have been installed. In particular, in the course of two expeditions within the Italian Scientific Project PNRA, during the 2003-2004 and 2005-2006 austral summers, we installed 9 broadband temporary seismic stations (blue circles in Figure 2) all equipped with Trillium T40 sensors and powered by solar panels and batteries. All the stations were located around the David Glacier along two main alignments running from the coast to the TAM and cutting the chain perpendicularly, covering an area of 100x150 Km^2. One of these stations (STAR, cyan triangle) become permanent at the end of the first expedition and it has been still working on. This setting allows us to have data for at least 2 months at each station.

We analysed records of teleseismic events occurring between 2003 and 2007, with magnitude greater than 5.5 and epicentral distance between 85° and 120°. This distance range guarantees the presence and easy identification of the SKS arrival. The 5-year dataset is complete only for permanent stations.

SINGLE SHEAR-WAVE SPLITTING MEASUREMENTS

The fast axes orientation and the delay time between faster and slower phases are the two parameters provided by shear-wave splitting analysis. Most methods start assuming the anisotropic medium composed by one single layer with horizontal symmetry axis.

The fast velocity direction (ϕ) corresponds to the direction along which strain aligns the minerals; the delay time (*dt)* allows to estimate the thickness of the anisotropic material. We retrieved these two parameters using the *Silver and Chan* [1991] method. This is based on a grid search over the possible splitting parameters that better remove the effects of anisotropy from the waveforms. In a general case, this can be done searching the most singular covariance matrix based on its eigenvalues λ_1 and λ_2. A special case is when the initial wave polarization is known, as for SKS and SKKS phases, and when the signal-to-noise level is low; in this case the splitting parameters can be recovered minimizing the energy on the transverse component.

We used the SPLITLab environment [*Wustefeld et al.*, 2008], a Matlab graphical user interface (GUI) that allows the analysis of shear-wave splitting for huge amounts of data and the quality check on the results. In addiction, SPLITLab provides a method to calculate simultaneously shear-wave splitting parameters using the eigenvalues approach (EV), minimization of energy on the transverse component (SC) and rotation-correlation technique (RC) [*Fukao,* 1984*; Bowman and Ando,* 1987]. The last method removes the effect of splitting, maximizing the cross-correlation coefficient between radial (Q) and transverse (T) components of the waveforms

228 in the selected windows.

229

230 As the initial polarization of the wave is assumed to be radial, RC and SC methods are applicable
231 to phases as SKS and SKKS; the EV method instead uses the back-azimuth as initial polarization
232 of the wave and therefore it is applicable only for S phases. Synthetics tests on the RC and SC
233 methods [*Wustefeld and Bokelmann*, 2007] demonstrate comparable results when fast axes is far
234 enough from the back-azimuth direction but shown very different behaviours when the
235 back-azimuth is close to the fast or slow direction (null directions). In this case the RC method
236 deviates by 45º from the input fast axis, while the SC method yields scattered estimates around it.
237 Therefore a comparison of results between these two methods distinguishes null measurements
238 from the real splitting cases and allows us to assign a quality flag for any single measurement
239 [*Wustefeld and Bokelmann*, 2007].

240

241 More specifically, we define the following parameters:

242

243 $\Delta\Phi=\Phi_{SC}-\Phi_{RC}$ and

244 $\rho=dt_{RC}/dt_{SC}$.

245

246 and we pick "true" splitting measurements only if the following conditions are satisfied
247 simultaneously:

248

249 1) $\rho>0.7$

2) $|\Delta\Phi| < 22.5^{o}$

3) Signal-to-noise ratio (SNR) on the transverse component greater than 3

The measurement is flagged as "good" when $\Delta\Phi<8^{o}$ and $0.8<\rho<1.1$, "fair" when $\Delta\Phi<15^{o}$ and $0.7<\rho<1.2$ and "poor" in all other cases.

We consider null a measurement when S-wave travelling through the medium has no splitting. This happens when the medium is isotropic or when the wave propagates along the so called null direction, that is the direction for which the initial wave polarization is parallel to the fast or slow axis [*Savage*, 1999]. For SKS and SKKS cases, these directions coincide with the back-azimuth of the selected event. As suggested by *Wustefeld and Bokelmann* [2007], we can consider null a measurement when $\Delta\Phi \sim n*45^{o}$ (with n an integer) and small ρ; we consider "good nulls" when $37^{o}<\Delta\Phi<53^{o}$ and $0<\rho<0.2$, "fair nulls" when $32^{o}<\Delta\Phi<58^{o}$ and $0<\rho<0.3$ and "poor nulls" in all other cases or when the SNR is lower than 3.

In the following we will consider only the SC measurements and we compare them with the results of RC method for the quality assignment only.

Single station-event measurements obtained with the *Silver and Chan* [1991] method are mapped on Figure 3 and listed on Table S2 (only splitting measurements) and Table S3 (only null measurements) of the auxiliary materials. For the sake of simplicity, in red we have plotted measurements flagged as “good” and in orange those flagged as “fair”; all measurements are

projected at a piercing point of 150 Km depth. In the map on the left splitting measurements are plotted as segments parallel to fast axes and scaled to delay time; in the map on the right nulls are plotted as crosses parallel and perpendicular to the back-azimuth of the analysed events.

Totally, we have 94 good and 44 fair splitting and 33 good and 37 fair null measurements. The distribution of these data is very scattered (Figure 3). NNE-SSW seems to be the most frequent fast direction but also NNW-SSE or N-S measurements are well visible. For some stations we have measurements perpendicular to each other as an expression of the possible presence of a complex anisotropic structure beneath the region. Nulls measurement distribution is in agreement with this single-splitting pattern.

Easier to follow is the distribution of average values of splitting measurements, done for any single station (Figure 4 and Table S4). When possible, the average values were calculated using good and fair measurements (dark blue segments) but in a few cases only fair measurements were used (cyan segments). In all cases nulls are excluded. Due to lack of results in JYCE and MORR, no average measurement is calculated for these two stations. Most of the stations (TNV, VNDA, TRIO, HUGH) show a NE-SW direction and delay time values often comparable among them and in agreement with previous works. Station STAR has average anisotropy with a NNW-SSE direction while in OHG it is N-S with a lower value of delay time. Stations with average anisotropy calculated with fair measurements (PHIL, PRST, and MDAN) show a uniform NNE-SSW direction, quite different with respect to those around.

294 The distribution of these measurements is comparable with previous works [*Barklage et al.*,
295 2009; *Pondrelli et al.*, 2005]. Our results however seem to estimate larger values of delay time; in
296 fact, compared to the average values of 1 and 1.6 s calculated in the past, for most of our stations
297 we also find values larger than 2 s and only at OHG we have a smaller delay time (1.5 s).
298
299
300

VERTICAL CHANGES OF THE ANISOTROPY

The transverse energy minimization (SC) and rotation-correlation (RC) techniques described above allow the calculation of the splitting parameters based on a few assumptions on the structure of the anisotropic medium to analyse. The anisotropic medium is supposed to have one single anisotropic layer with anisotropy oriented along its horizontal axis. The splitting parameters give a true value if the earth structure is really composed as the initial model, while they give an "apparent" result if the real earth model beneath the study site includes two or more anisotropic layers or the symmetry axis is not horizontal. A periodicity on the splitting parameters pattern with respect to the back-azimuth of the events usually indicates the presence of greater complexity [*Savage*, 1999; *Menke and Levin*, 2003].

To focus on the possible meaning of the scattering we obtain in our measurements, we studied the distribution of splitting parameters with respect to the back-azimuth of teleseismic earthquakes. Examples for VNDA, STAR and TNV are showed on Figure 5. In the plots, good (red crosses) and fair (blue crosses) splitting measurements and good (red circles) and fair (blue squares) null measures are mapped. The distribution of fast axis and delay time with respect to the back-azimuth seems to fit with different types of two-layer models (represented by green lines). The distribution of earthquake's back-azimuth is however discontinuous; for most events, phases under study come from NW or SE quadrants while the other back-azimuths are absent. Therefore a unique interpretation would be rash and unreliable.

323 To test vertical variation of anisotropy in a different way, we use a cross-convolution technique
324 [*Menke and Levin*, 2003] to model all waveforms simultaneously and re-build the complex
325 pattern of our measurements; we try to fit the data with an adequate two-layer model.
326 The technique consists of two steps; first, splitting parameters for each event are calculated
327 maximising the cross-correlation between horizontal rotated seismograms. Only events with a
328 cross-correlation estimator value greater than 0.8 and modelled polarization within the error range
329 of 20° are picked for the following step. These criteria are so selective that only a small portion of
330 data can be used for the inversion, generally about 8-9% of the complete dataset for each station.
331 For this reason the inversion was done only for permanent stations TNV and VNDA and for those
332 temporary stations having a wide range of day-recordings, namely STAR and OHG. The final
333 solutions have been obtained using a minimum of 4 (OHG) and a maximum of 24 (VNDA)
334 events.
335 In the second step we find the unique earth model structure that satisfies the entire group of
336 observations with a grid-search inversion using a cross-convolution technique. Results are
337 represented as error surface plot as showed on Figure S1 (auxiliary material). The more complex
338 model is chosen considering the distribution of the models on error surface plots and on the misfit
339 reduction. Where the best is a double layer model, the final solution is selected excluding those
340 with delay time equal to 3.0 sec (and above) and differences between two layer fast axes
341 orientations ranging between 80° and 100°. This choice avoids near-normal fast polarization
342 values whereby delay time in one layer cancels the delay time in the other [*Menke and Levin*,
343 2003].
344

345 The modelling results are mapped in Figure 4 and listed on Table S5 (auxiliary material).
346 Solutions for stations where one layer earth structure fits the waveforms better than a
347 double-layer model are mapped with the violet sticks oriented parallel to the fast axis and scaled
348 with the delay time. Stations for which the double layer is the best model are represented with
349 two colours: red for the lower and black for the upper layer. For each station the 10 solutions with
350 lowest misfit are plotted.
351
352 Beneath VNDA and TNV stations, located respectively on the southern and northern margin of
353 the region, a vertical variation of the anisotropy is absent. From the inversion we obtained that
354 beneath TNV the dominant anisotropy shows fast direction between 41° and 44° and delay time
355 between 1.1 and 1.2 s. For VNDA the situation is similar, with a fast direction between 36° and
356 39° and the delay time range between 1.0 to 1.1 s. These values are consistent with the NE-SW
357 alignment found for the averaged measurements and with previous papers.
358
359 On the other hand, the two-layer anisotropic model is the best fitting for stations STAR and
360 OHG. These sites are located on structurally different places: STAR is along the coast while
361 OHG is inland, but the anisotropy shows similar patterns. Underneath STAR the fast axis for the
362 lower layer varies from 100° to 150° and delay time from 0.9 to 2.3 s; in the upper layer
363 respective intervals are -10° to 40° and 0.9 to 2.2 s. Beneath OHG, fast axis for lower layer varies
364 in the range from 120° to 150°, delay from 1.2 to 1.6 s; for the upper layer directions are from
365 -10° to 20° and dt from 1.7 to 2.9 s. All these measurements are consistent among them and for
366 the upper layers (black sticks) we show the same orientation obtained for closer stations.

LATERAL CHANGES IN THE ANISOTROPY DIRECTION

Results obtained for the two permanent stations TNV and VNDA show scattering in the single event-station measurements, but absence of evidence for multi-layer structure. We decided to focus on the hypothesis of lateral changes of the anisotropy direction at depth as a possible interpretation of our measurements.

The computation of Fresnel zones, such as suggested by *Alsina and Snieder* [1995], helps to identify the presence of different patterns of anisotropies sampled from rays coming to the same stations from different back-azimuths. Taking into account where the rays have a common path beneath the station it is possible to identify the depth interval at which this change occurs (Figure 6).

The elastic wave generated by an earthquake is influenced by physical properties of the earth in the vicinity of the geometrical ray path. This ray path can be schematized as a tube, the diameter of which is the Fresnel zone. The size of the Fresnel zone is a function of the wave frequency, and distance along the ray. For a steep-incidence phase, such as SKS or SKKS, it is then a function of the depth beneath the receiver.

The Fresnel zone at the depth h, can be calculated using [*Pearce and Mittleman*, 2002]:

$$Rf = \frac{1}{2}\sqrt{T\nu h}$$

where Rf is the radius of the Fresnel zone expressed in Km, T is the dominant period of the wave and ν is the wave velocity. We choose T=10 s as the dominant period of the wave, with the

388 corresponding shear-wave velocity of S phase obtained from IASP91 model (3.75Km/s at 35Km,
389 4.476 Km/s at 50 Km, 4.49 Km/s at 100 Km, 4.45Km/s at 150 Km, 4.5 Km/s at 200 Km and 4.6
390 Km/s at 250 Km).
391 Examples for VNDA and TNV stations are shown in Figure 6; for each station we mapped the
392 shear-wave splitting direction obtained studying two events coming from opposite
393 back-azimuths. The two rays visibly sample different anisotropic patterns. If we take into
394 account that these two rays share the same path beneath the station (see sketch included in Figure
395 6), the lateral change in the anisotropy should lay deeper than their conjunction point (Z depth on
396 the inset). Indeed, below this depth the rays sample different patches (blue circles on Figure 6)
397 and above this depth the rays travel through the same anisotropic medium (yellow circles). The
398 Fresnel zones are calculated for 35, 50, 100, 150, 200, 250 Km of depth. The shared paths are
399 represented by circles of opposite rays which cross each others, and the paths along which rays
400 are separated (thus, sampling different anisotropies) are represented by circles that do not cross.
401 We can deduce that for VNDA the lateral variation on the anisotropic properties occurs between
402 50 and 100 Km of depth while beneath TNV it occurs a bit deeper, between 100 and 150 Km of
403 depth.
404
405 When we analyse rays coming from NW at both permanent stations, we obtain similar results,
406 which indicate a dominant NE-SW anisotropy direction beneath the TAM. This is in effect the
407 most recurrent direction measured for the region with no dependency on the recovery method.
408 On the contrary, rays coming from east seem to sample different anisotropy structures at the two
409 sites - WNW-ESE for TNV and NW-SE for VNDA. These observations take definitely trace of

two distinct anisotropic behaviours characterizing the TAM and the Ross Sea Embayment.

412 **DISCUSSION**

413

414 Figure 7 summarizes all our shear-wave splitting results (in colour) in the Victoria Land zone; for
415 comparison we add measurements obtained by previous studies (in grey). The figure indicates the
416 presence of discontinuous domains of anisotropy in the Victoria Land region.
417 At station TNV (Northern region) we have a general agreement between different measurements.
418 The NE-SW trend found by *Pondrelli et al.* [2005] and lately confirmed by *Barklage et al.* [2009]
419 is in agreement with both our average of single measurements (blue stick) and our group
420 inversion model (violet stick). However, the last analysis suggests that the scattering in single
421 measurements should not be ascribed to a vertical change in the anisotropy direction, at least at
422 lithosphere-astenosphere structure scale. The Fresnel zone computation shows that a lateral
423 variation at depth beneath TNV justifies the splitting directions moving away from the dominant
424 NE-SW.
425 In the southern region we have a similar situation. Results for VNDA station are in agreement
426 among them and with the splitting directions obtained for the temporary TAMSEIS network (in
427 gray). The NE-SW direction is generally confirmed also moving towards north. Again, the group
428 inversion on our data excludes a vertical change in anisotropy directions beneath VNDA (at least
429 at the scale we can investigate), while Fresnel zone analysis supports the possibility of a lateral
430 change at depth. This allows us to justify the single measurements trending away from the main
431 NE-SW direction.
432 Some estimates for the thickness of the anisotropic layer in the area can be inferred from delay
433 time values of the grouped inversions. In both North and South Victoria Land, delay time ranges

434 between 1.0 to 1.2 s. Considering that *Lawrence et al.* [2006c] estimate 1 s delay time for a 150
435 Km thick anisotropic medium, with 3% anisotropy, we can infer that the thickness of the
436 anisotropic layer should vary from 150 and 180 Km.
437 From the calculation of the Fresnel zone, we can affirm that the anisotropic material should lay at
438 a depth larger than 50-100 Km (smaller values obtained respectively for VNDA and TNV),
439 therefore the anisotropy thickness become in general greater than 200 Km in depth. Since the
440 lithosphere thickness beneath the Ross embayment was calculated in 250 Km [*Morelli and*
441 *Danesi*, 2004], anisotropy would be partially located in the lower lithosphere, with a possible
442 contribution to the astenospheric's mantle.
443
444 The central part of the region has different features. The first difference is the direction of average
445 measurements in OHG and STAR, which are N-S and NNW-SSE respectively. The mean
446 directions calculated using only fair measurements (light blue stick on Figure 7) follow the same
447 pattern.
448 Group inversion here gives a two-layer anisotropic model with NW-SE direction for the lower
449 layer and N-S for the upper one. Since OHG is located on thick crust (about 35 Km) [*Lawrence et*
450 *al.*, 2006c] and STAR on thinner crust (about 20 Km), and considering that the anisotropy
451 direction shows the same pattern, it is reasonable to expect that the anisotropy distribution is
452 independent from the shallow structure, excluding (or limiting) a possible crustal contribution.
453 Delay time values vary between 1.2-1.6 s and 0.9-2.3 s in the lower layers and between 1.7-2.9
454 and 0.9-2.2 s in upper ones for OHG and STAR respectively, providing estimates for anisotropy
455 thickness of 435-675 Km beneath OHG and 270-675 Km beneath STAR. Considering that the

456 lithosphere thickness is approximately 250 Km, we can infer an asthenospheric contribution.
457
458 From these results it appears that a narrow zone separates a dominant NE-SW anisotropy of the
459 Northern and Southern areas from the double layer structure inferred for stations closer to the
460 David Glacier. Dominant directions for upper and lower layers are N-S and NW-SE respectively.
461 The first orientation is in agreement with results found at some stations of the TAMSEIS array
462 (gray sticks on Figure 7) while the second direction matches with some single measurements
463 close to station TNV (gray sticks on Figure 7) [*Pondrelli et al.*, 2005].
464 TRIO and HUGH, temporary stations located in the central part of the study region, have a
465 NE-SW mean value. On these sites however we could not apply group inversion or the Fresnel
466 zone technique for lack of usable data.
467
468 Our measurements of anisotropy can be easily related to the tectonic features in the area which
469 indicate that crust and sub-continental mantle deform coherently (Vertically Coherent
470 Deformation, VCD, as defined by [*Silver*, 1996]). The basic idea is that when more than one
471 deformational event occurs, the effect of the younger is recorded on the hotter and deeper layer,
472 while the oldest event remains recorded in the shallower and colder layer. With this concept in
473 mind, we can interpret the double layer anisotropic structure: the N-S direction of shallow
474 anisotropy would be related to the deformation occurred during the second phase of extension
475 (55-32 Ma), and the lower layer anisotropy would be related to the last transtensional event, that
476 is still going on (32 Ma to the Present). In this context the NE-SW anisotropy can be interpreted
477 as frozen-in anisotropy relative to older geological events as inferred by several authors

[*Barklage et al.*, 2009; *Pondrelli et al.*, 2005], overprinted locally by more recent tectonic events. This hypothesis would also agree with possible lateral variations at depth. In fact, the contribution from western paths is in agreement with the NE-SW frozen-in anisotropy that would be beneath the TAM chain. More recent tectonic events have been taking place mainly in the Ross Sea, beneath which we sample WNW-ESE to N-S anisotropy directions.

Our measurements could also indicate an absolute plate motion (APM) contribution. The APM for the Antarctic plate on the Victoria Land region is N18W (green arrow on Figure 7; [*Gripp and Gordon*, 2002]), that is quite similar to the lower layer anisotropy direction. We therefore could deduce that the frozen-in anisotropy existing in the upper layer is linked to the two extensional phases of the Ross Orogeny and the APM contribution is constrained in the lower layers. This hypothesis has been already investigated by *Kendall et al.* [2002] studying seismic anisotropy on continental environments as the Canadian shield. However, we should remind that the low velocity of the Antarctica plate (1.3-1.6 mm/yr) usually does not produce the strain needed to generate this amount of anisotropy and therefore, in agreement with *Barklage et al.* [2009], we use this hypothesis as alternative solution.

CONCLUSIONS

Shear-wave splitting measured in the Victoria Land region indicates that the NE-SW anisotropic direction is the most frequent orientation of anisotropy for stations located on northern and southern domains of the study region, in agreement with previous measurements. Here we add some new data supporting the presence of a lateral variation at depth, represented by a main NE-SW anisotropy direction beneath the TAM and some indications of a WNW-ESE to NW-SE anisotropy beneath the Ross Sea. For stations located around the David Glacier the distribution of single measurements is more scattered and the grouped inversion shows the presence of a double anisotropic layer for the central area of the Victoria Land. N-S and NNW-SSE are the two dominant directions respectively for the upper and lower layer, in agreement with the direction of most of the tectonic structures in the area, presumably generated during the Ross Orogeny deformational phases.

Despite the dataset incompleteness, this work has provided a good sketch of the regional seismic anisotropy pattern, including new heterogeneities and an original detailed view for the Victoria Land. The possibility of significant improvements in the database in the course of new field campaigns is to be hoped in order to go deeper in the comprehension of these results.

AKNOWLEDGMENTS

This work is supported by Programma Nazionale di Ricerche in Antartide (PNRA). All figures have been produced with GMT package [*Wessel and Smith*, 1991; 1998]

REFERENCES

Alsina, D., and R. Snieder (1995), Small-Scale Sublithospheric Continental Mantle Deformation - Constraints from Sks Splitting Observations, *Geophys J Int*, *123*(2), 431-448.

Anderson, J. B. (1999), *Antarctic Marine Geology*, Cambridge University Press, Cambridge.

Bannister, S., et al. (2003), Variations in crustal structure across the transition from West to East Antarctica, Southern Victoria Land, *Geophys J Int*, *155*(3), 870-884.

Barklage, M., et al. (2009), Upper mantle seismic anisotropy of South Victoria Land and the Ross Sea coast, Antarctica from SKS and SKKS splitting analysis, *Geophys J Int*, *178*(2), 729-741.

Bayer, B., et al. (2007), Seismic anisotropy beneath dronning maud land, antarctica, revealed by shear wave splitting, *Geophys J Int*, *171*(1), 339-351.

Behrendt, J. C. (1999), Crustal and lithospheric structure of the West Antarctic Rift System from geophysical investigations — a review, *Global and Planetary Change*, *23*(1-4), 25-44.

Bentley, C. R. (1991), Configuration and structure of the subglacial crust, in *The Geology of Antarctica*, edited by R. J. Tingey, pp. 335-364, Oxford University Press, New York.

Bowman, J. R., and M. Ando (1987), Shear-wave splitting in the upper-mantle wedge above the Tonga subduction zone, *Geophysical Journal of the Royal Astronomical Society*, *88*(1), 25-41.

Dalziel, I. W. D., and D. H. Elliot (1982), West Antarctica: Problem child of Gondwanaland, *Tectonics*, *1*(1), 3-19.

Danesi, S., and A. Morelli (2001), Structure of the upper mantle under the Antarctic Plate from surface wave tomography, *Geophysical Research Letters*, *28*(23), 4395-4398.

Fitzgerald, P. G. (1992), The Transantarctic Mountains of Southern Victoria Land - the Application of Apatite Fission-Track Analysis to a Rift Shoulder Uplift, *Tectonics*, *11*(3), 634-662.

Fukao, Y. (1984), Evidence from Core-Reflected Shear-Waves for Anisotropy in the Earths

Mantle, *Nature*, *309*(5970), 695-698.

Gripp, A. E., and R. G. Gordon (2002), Young tracks of hotspots and current plate velocities, *Geophys J Int*, *150*(2), 321-361.

Karato, S., et al. (2008), Geodynamic significance of seismic anisotropy of the upper mantle: New insights from laboratory studies, *Annual Review of Earth and Planetary Sciences*, *36*, 59-95.

Kendall, J. M., et al. (2002), Seismic heterogeneity and anisotropy in the western Superior Province, Canada; insights into the evolution of an Archaean craton, in *The early Earth; physical, chemical and biological development*, edited by C. M. R. Fowler, et al., pp. 27-44, Geological Society Special Publications, London, United Kingdom (GBR).

Lawrence, J. F., et al. (2006a), Upper mantle thermal variations beneath the Transantarctic Mountains inferred from teleseismic S-wave attenuation, *Geophysical Research Letters*, *33*(3), -.

Lawrence, J. F., et al. (2006b), Crust and upper mantle structure of the Transantarctic Mountains and surrounding regions from receiver functions, surface waves, and gravity: Implications for uplift models, *Geochemistry Geophysics Geosystems*, *7*, -.

Lawrence, J. F., et al. (2006c), Rayleigh wave phase velocity analysis of the Ross Sea, Transantarctic Mountains, and East Antarctica from a temporary seismograph array, *J Geophys Res-Sol Ea*, *111*(B6), -.

Lythe, M. B., et al. (2001), BEDMAP: A new ice thickness and subglacial topographic model of Antarctica, *J Geophys Res-Sol Ea*, *106*(B6), 11335-11351.

Menke, W., and V. Levin (2003), The cross-convolution method for interpreting SKS splitting observations, with application to one and two-layer anisotropic earth models, *Geophys J Int*, *154*(2), 379-392.

Morelli, A., and S. Danesi (2004), Seismological imaging of the Antarctic continental lithosphere: a review, *Global and Planetary Change*, *42*(1-4), 155-165.

Muller, C. (2001), Upper mantle seismic anisotropy beneath Antarctica and the Scotia Sea region, *Geophys J Int*, *147*(1), 105-122.

Pearce, J., and D. Mittleman (2002), Defining the Fresnel zone for broadband radiation, *Physical Review E*, *66*(5), -.

571 Piana Agostinetti, N., et al. (2004), Crustal Structure of Northern Victoria Land from Receiver
572 Function Analysis, *Terra Antarctica*, *11*(1), 5-14.

573 Pondrelli, S., and R. Azzara (1998), Upper mantle anisotropy in Victoria Land (Antarctica), *Pure*
574 *and Applied Geophysics*, *151*(2-4), 433-442.

575 Pondrelli, S., et al. (2005), Seismic Anisotropy beneath Northern Victoria Land from SKS
576 splitting Analysis, in *Antarctica: Contributions to global eart sciences*, edited by D. K. Futterer,
577 et al., pp. 153-160, Springer-Verlag, Berlin Heidelberg, New York.

578 Reading, A. M., and M. Heintz (2008), Seismic anisotropy of East Antarctica from shear-wave
579 splitting: Spatially varying contributions from lithospheric structural fabric and mantle flow?,
580 *Earth and Planetary Science Letters*, *268*(3-4), 433-443.

581 Ritzwoller, M. H., et al. (2001), Crustal and upper mantle structure beneath Antarctica and
582 surrounding oceans, *J. Geophys. Res.*, *106*(B12), 30,645-630,670.

583 Salvini, F., and F. Storti (1999), Cenozoic tectonic lineaments of the Terra Nova Bay region,
584 Ross Embayment, Antarctica, *Global and Planetary Change*, *23*(1-4), 129-144.

585 Savage, M. K. (1999), Seismic anisotropy and mantle deformation: What have we learned from
586 shear wave splitting?, *Reviews of Geophysics*, *37*(1), 65-106.

587 Silver, P. G., and W. W. Chan (1991), Shear-Wave Splitting and Subcontinental Mantle
588 Deformation, *J Geophys Res-Sol Ea*, *96*(B10), 16429-16454.

589 Silver, P. G. (1996), Seismic anisotropy beneath the continents: Probing the depths of geology,
590 *Annual Review of Earth and Planetary Sciences*, *24*, 385-&.

591 Studinger, M., et al. (2004), Sub-ice geology inland of the Transantarctic Mountains in light of
592 new aerogeophysical data, *Earth and Planetary Science Letters*, *220*(3-4), 391-408.

593 ten Brink, U. S., et al. (1997), Uplift of the Transantarctic Mountains and the bedrock beneath
594 the East Antarctic ice sheet, *J. Geophys. Res.*, *102*(B2), 27,603–627,621.

595 Tingey, R. J. (1991), *The Geology of Antarctica*, Oxford University Press, New York.

596 Wessel, P., and W. H. F. Smith (1991), Free software helps map and display data, *EOS Trans.*
597 *AGU*, *72*(41), 441.

598 Wessel, P., and W. H. F. Smith (1998), New, improved version of generic mapping tools
599 released, *EOS Trans. AGU*, *79*(47), 579.

600 Wustefeld, A., and G. Bokelmann (2007), Null detection in shear-wave splitting measurements,
601 *B Seismol Soc Am*, *97*(4), 1204-1211.

602 Wustefeld, A., et al. (2008), SplitLab: A shear-wave splitting environment in Matlab, *Comput*
603 *Geosci-Uk*, *34*(5), 515-528.
604
605

FIGURES

Figure 1: Map showing the elevation of the bedrock [*Lythe et al.*, 2001] in Antarctica and main structural and seismic regions. The zoomed map corresponds to the Victoria Land region.

Figure 2: Map showing broadband seismic stations operating in the Victoria Land region; cyan triangles are permanent stations (TNV, VNDA and STAR), blue circles are those temporary campaign. Yellow triangles represent the TAMSEIS project stations. In the same map previous shear-wave splitting measurements are showed; any segment is oriented parallel to the fast axis and scaled with delay time. In purple results from *Pondrelli et al.* [2005] plotted at a piercing point of 150 Km depth; in yellow results from *Barklage et al.* [2009] plotted at the surface.

Figure 3: Single splitting and null measurements obtained with *Silver and Chan* [1991] method. In both maps good (in red) and fair (in orange) measurements are plotted using a piercing point of 150 Km. Splitting measurements are plotted with line-segment oriented parallel to the fast axis and scaled with delay time; null measurements are plotted with two cross-line oriented parallel to the back-azimuth and perpendicular to it. Blue circles and cyan triangles locate the stations (see Figure 2 for colour meaning).

Figure 4: Average measurements (dark blue and cyan) and results of grouped inversion (violet and red-black sticks) calculated for each station are shown on the map. Average measurements:

626 results in blue are calculated using good and fair measurements while in cyan are those obtained
627 with only fair measurements. Grouped Inversion: for each station the 10 best solutions, with
628 lowest misfit, are plotted. Violet segments represent one-layer best fitting model measures. Red
629 and black segments respectively indicate lower and upper measures for two-layer best fitting
630 models
631
632 Figure 5: Examples of back-azimuth dependence of the splitting parameters for VNDA, STAR
633 and TNV stations. Each panel contains good (red crosses) and fair (blue crosses) split
634 measurements and good (red circle) and fair (blue square) nulls measurements. Poor results are
635 excluded. Green lines on upper and medium panels correspond to the theoretical distribution of
636 two-layer model with splitting parameters described above each figure. The distribution of single
637 measurements is showed on lower plots.
638
639 Figure 6: Examples of Fresnel zones analysis for TNV and VNDA. Two events with opposite
640 back-azimuth and different splitting parameters are analysed. Different size on the circles
641 correspond to 35, 50, 100, 150, 200, 250 Km of depth of the Fresnel zone. In red we show the
642 splitting measurements plotted at 35 km of depth. All intersecting circles in yellow represent the
643 depth (Z on the inset) above which rays sampled the same anisotropy; in blue, separated circles
644 define the depth below which rays sampled mediums with different anisotropic properties.
645
646 Figure 7: Summary map of shear-wave splitting results. Mean values of the single shear-wave
647 splitting, calculated using good and fair split measurements, are in dark blue; mean values

calculated with only fair measurements are in light blue; results from group inversion where the best model is the single one (10 better solutions) are in violet; red and black are 10 better solutions for lower and upper layer respectively. Previous results of *Pondrelli et al.* [2005] and *Barklage et al.* [2009] are plotted in grey. The big green arrow indicates the absolute plate motion of the Antarctica plate [*Gripp and Gordon*, 2002]. Crustal thickness is taken from *Lawrence et al.* [2006b]

654

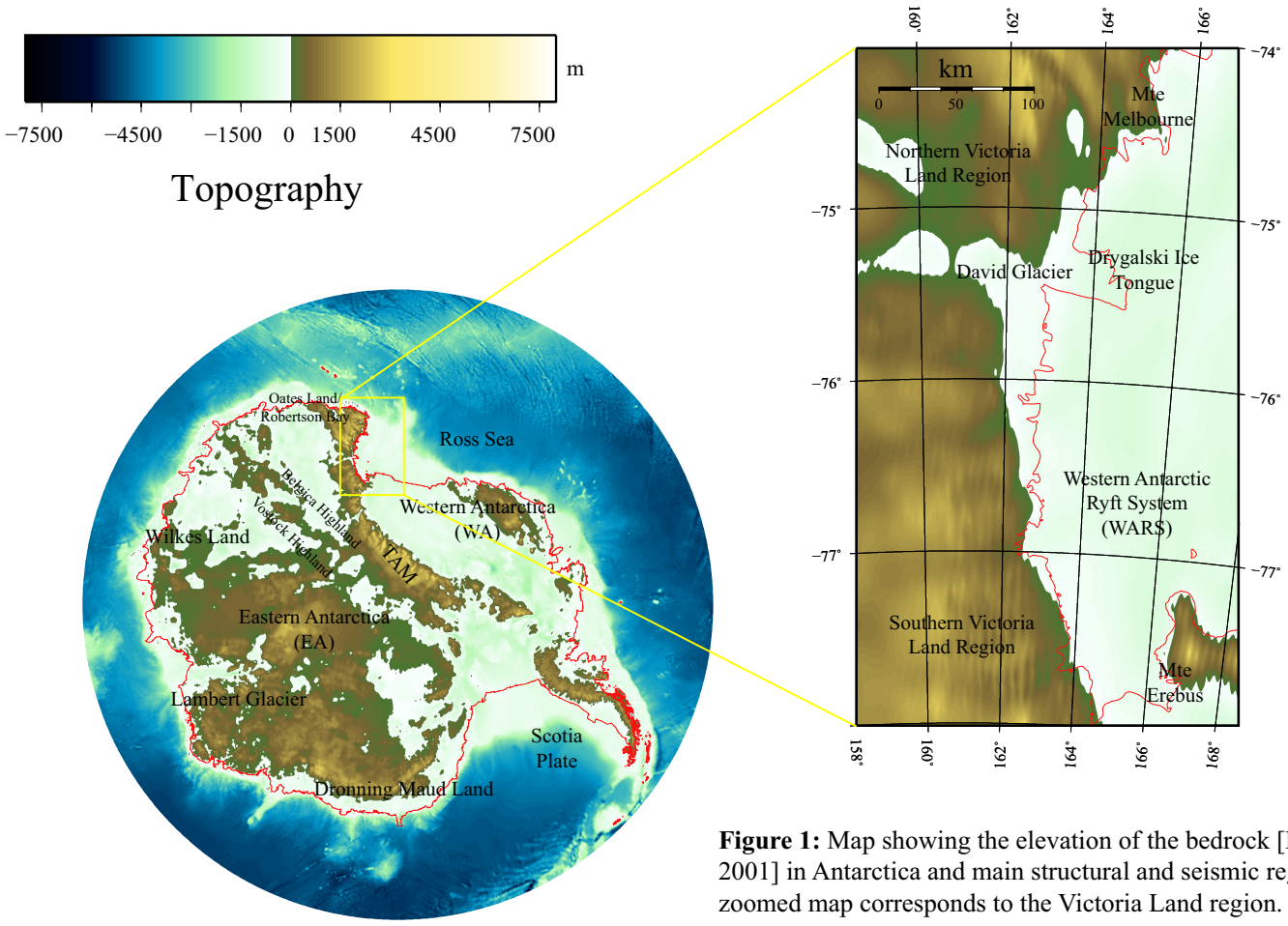

Figure 1: Map showing the elevation of the bedrock [Lythe et al., 2001] in Antarctica and main structural and seismic regions. The zoomed map corresponds to the Victoria Land region.

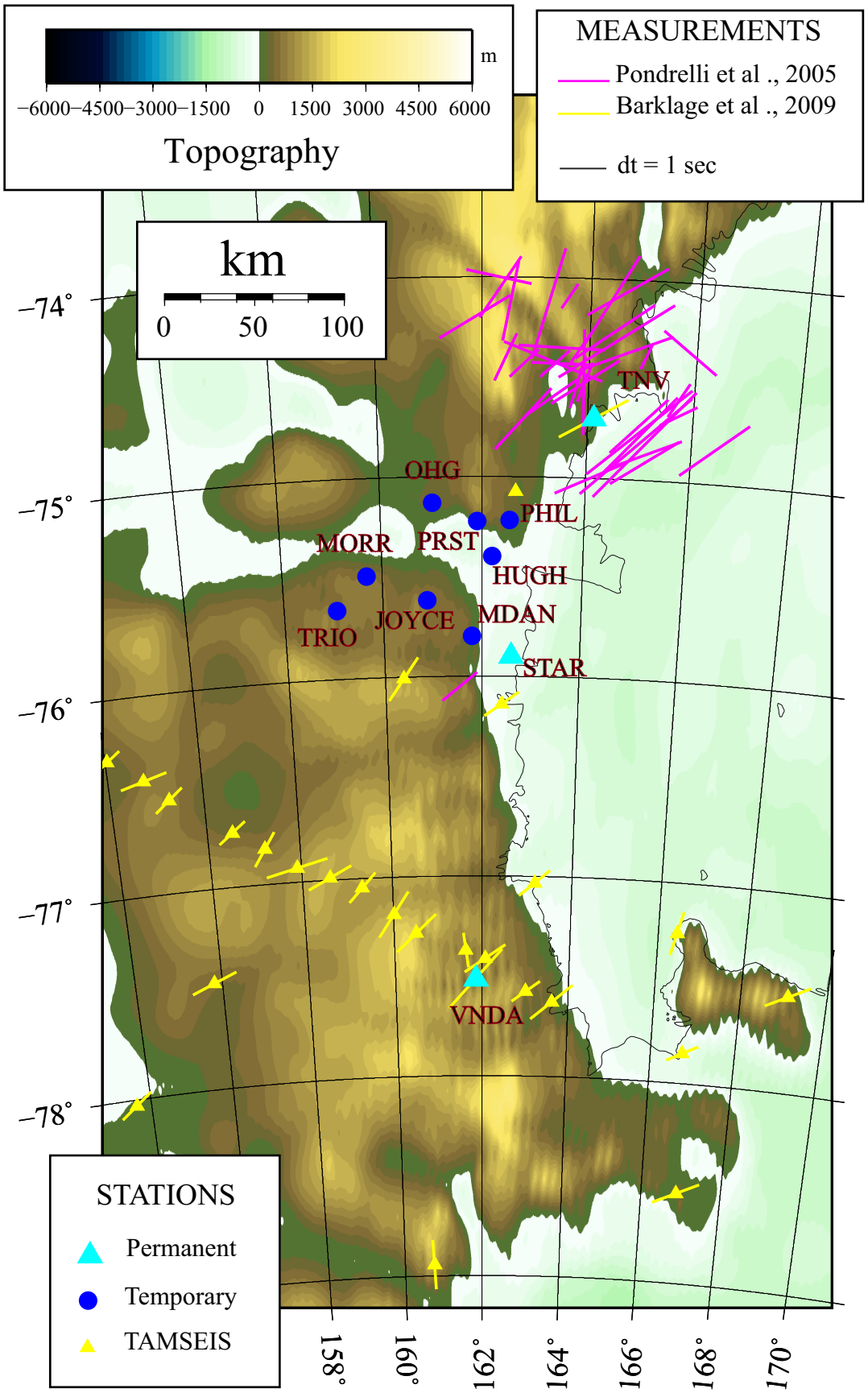

Figure 2: Map showing broadband seismic stations operating in the Victoria Land region; cyan triangles are permanent stations (TNV, VNDA and STAR), blue circles are those temporary campaign. Yellow triangles represent the TAMSEIS project stations. In the same map previous shear-wave splitting measurements are showed; any segment is oriented parallel to the fast axis and scaled with delay time. In purple results from Pondrelli et al. [2005] plotted at a piercing point of 150 Km depth; in yellow results from Barklage et al. [2009] plotted at the surface.

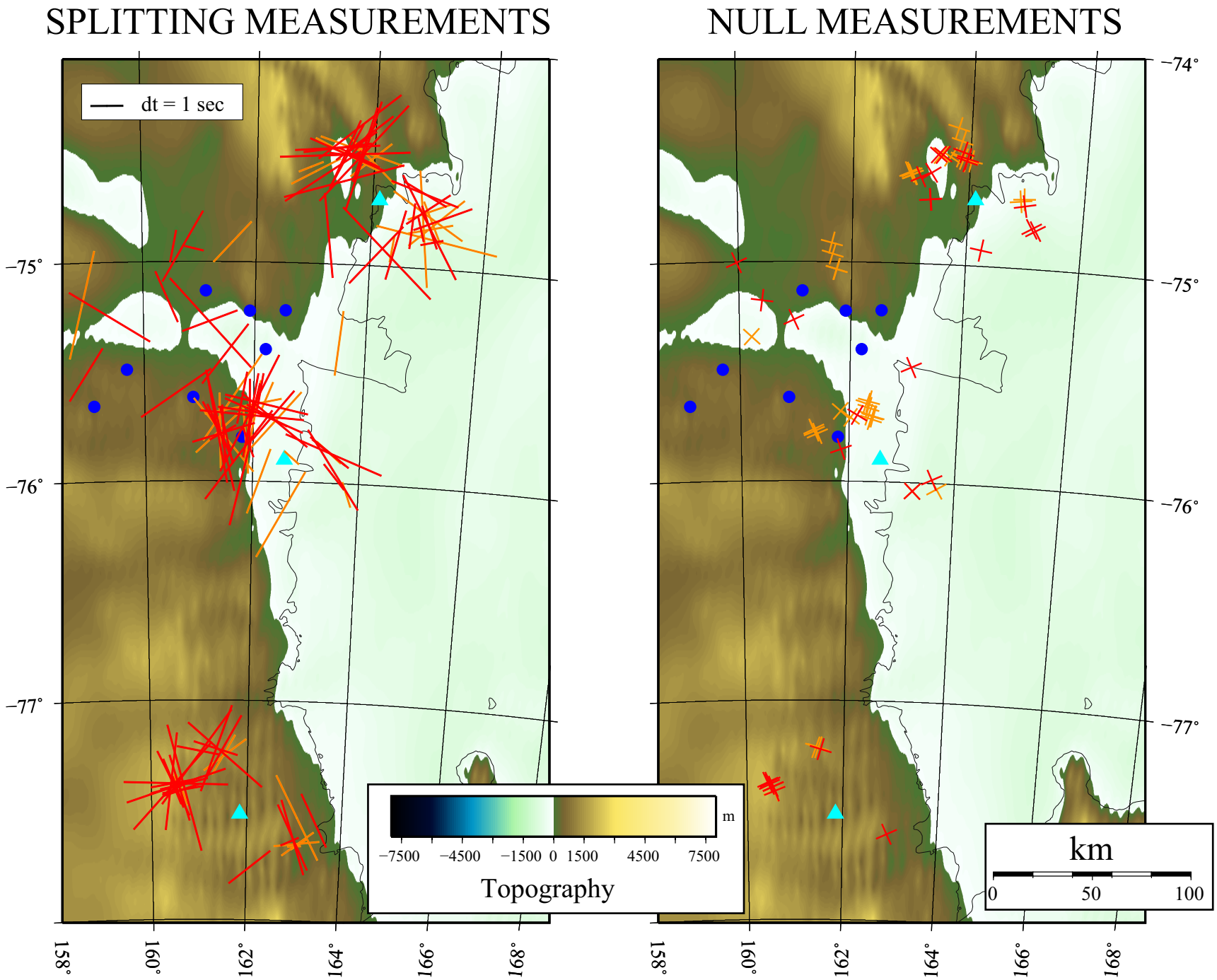

Figure 3: Single splitting and null measurements obtained with Silver and Chan [1991] method. In both maps good (in red) and fair (in orange) measurements are plotted using a piercing point of 150 Km. Splitting measurements are plotted with line-segment oriented parallel to the fast axis and scaled with delay time; null measurements are plotted with two cross-line oriented parallel to the back-azimuth and perpendicular to it. Blue circles and cyan triangles locate the stations (see Figure 2 for colour meaning).

Figure 4: Average measurements (dark blue and cyan) and results of grouped inversion (violet and red-black sticks) calculated for each station are shown on the map. Average measurements: results in blue are calculated using good and fair measurements while in cyan are those obtained with only fair measurements. Grouped Inversion: for each station the 10 best solutions, with lowest misfit, are plotted. Violet segments represent one-layer best fitting model measures. Red and black segments respectively indicate lower and upper measures for two-layer best fitting models.

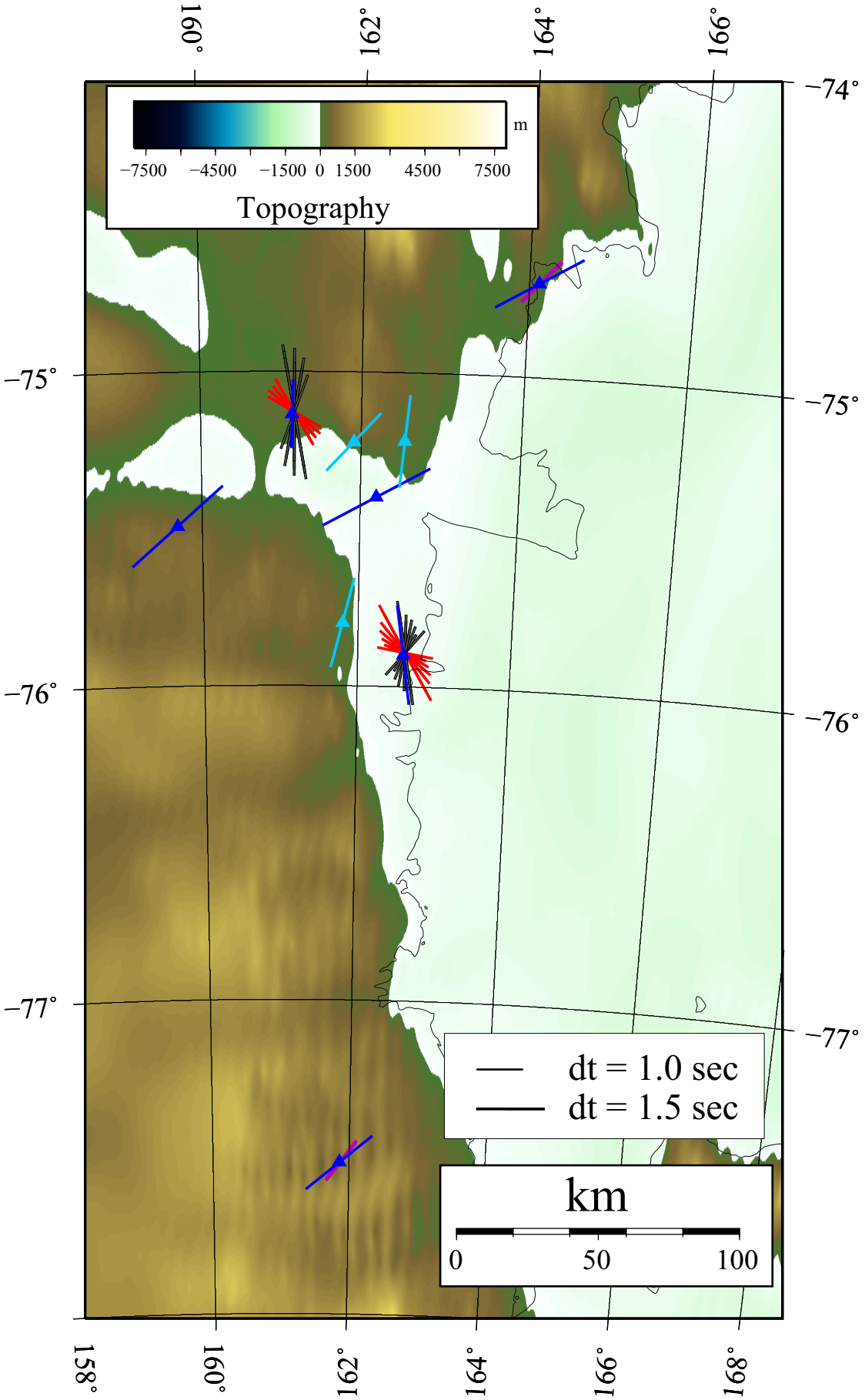

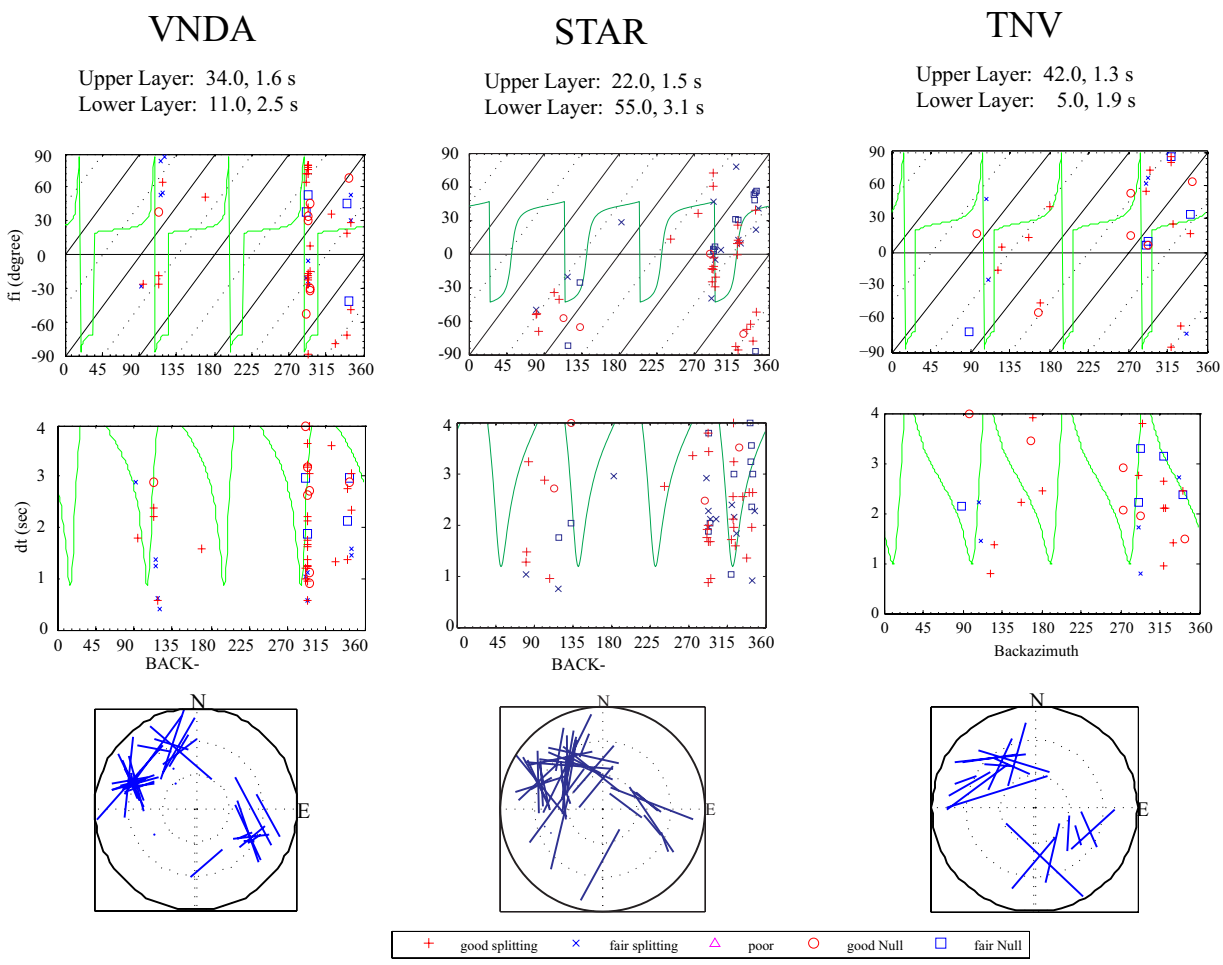

Figure 5: Examples of back-azimuth dependence of the splitting parameters for VNDA, STAR and TNV stations. Each panel contains good (red crosses) and fair (blue crosses) split measurements and good (red circle) and fair (blue square) nulls measurements. Poor results are excluded. Green lines on upper and medium panels correspond to the theoretical distribution of two-layer model with splitting parameters described above each figure. The distribution of single measurements is showed on lower plots.

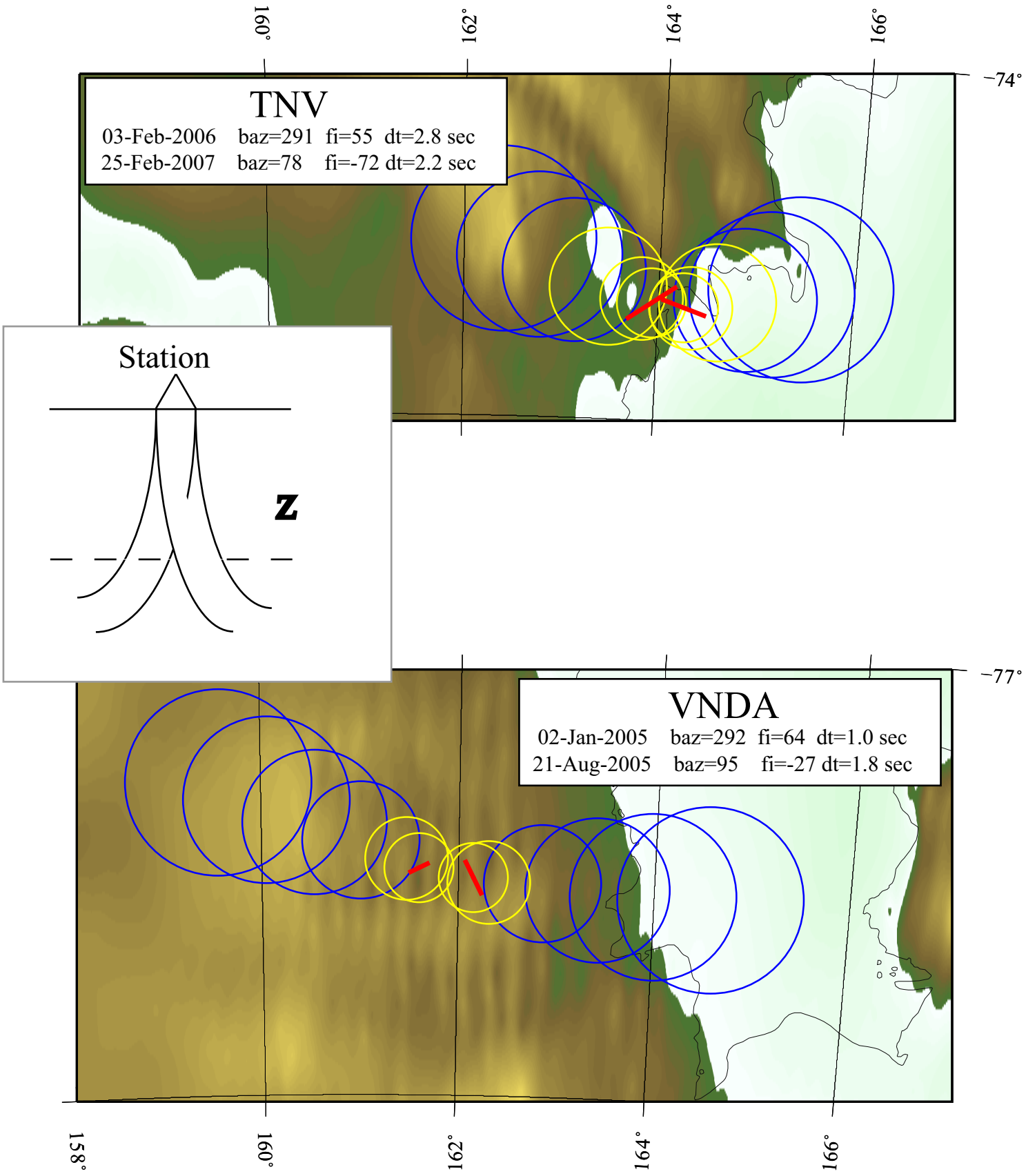

Figure 6: Examples of Fresnel zones analysis for TNV and VNDA. Two events with opposite back-azimuth and different splitting parameters are analysed. Different size on the circles correspond to 35, 50, 100, 150, 200, 250 Km of depth of the Fresnel zone. In red we show the splitting measurements plotted at 35 km of depth. All intersecting circles in yellow represent the depth (Z on the inset) above which rays sampled the same anisotropy; in blue, separated circles define the depth below which rays sampled mediums with different anisotropic properties.

Figure 7: Summary map of shear-wave splitting results. Mean values of the single shear-wave splitting, calculated using good and fair split measurements, are in dark blue; mean values calculated with only fair measurements are in light blue; results from group inversion where the best model is the single one (10 better solutions) are in violet; red and black are 10 better solutions for lower and upper layer respectively. Previous results of Pondrelli et al. [2005] and Barklage et al. [2009] are plotted in grey. The big green arrow indicates the absolute plate motion of the Antarctica plate [Gripp and Gordon, 2002]. Crustal thickness is taken from Lawrence et al. [2006b].

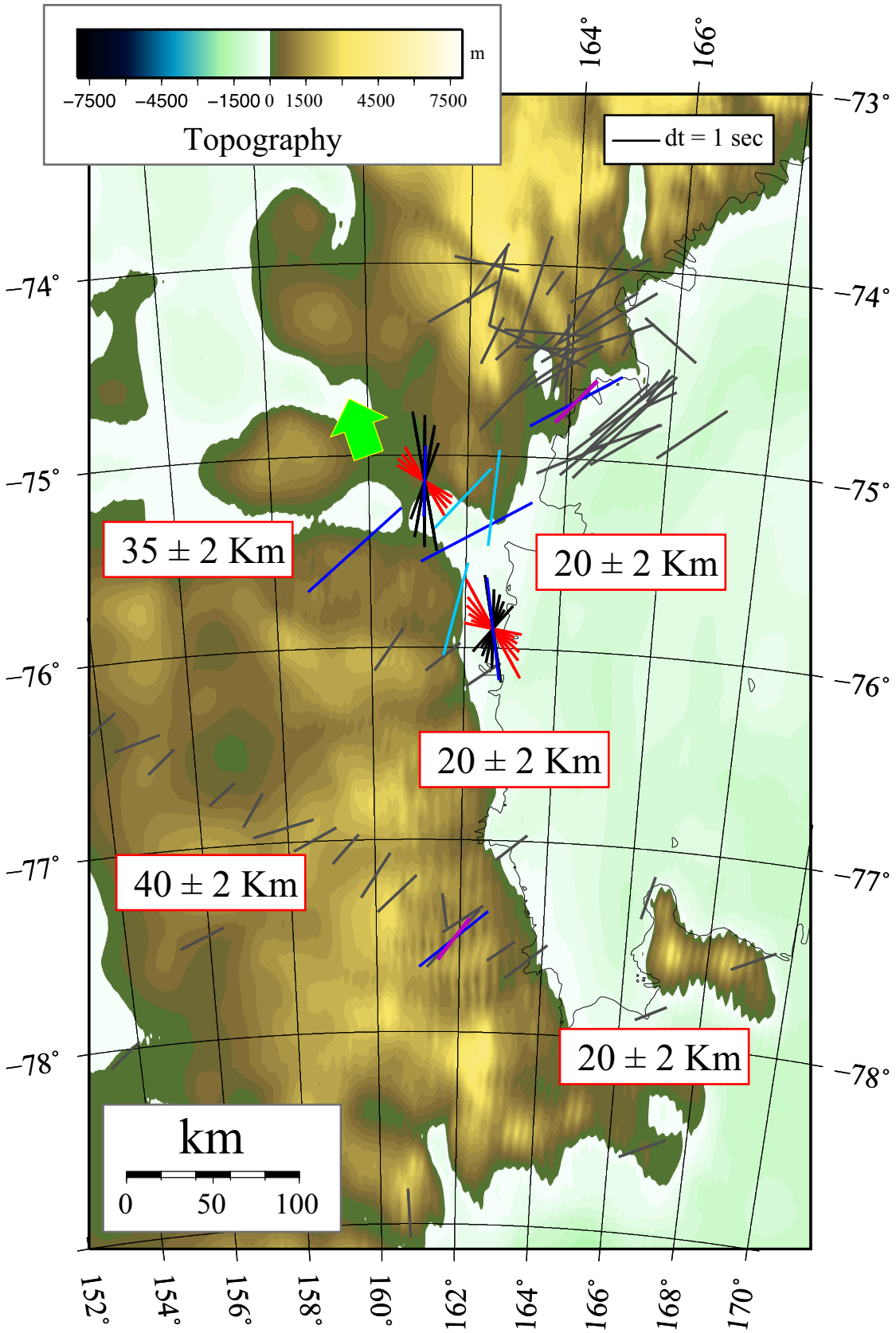

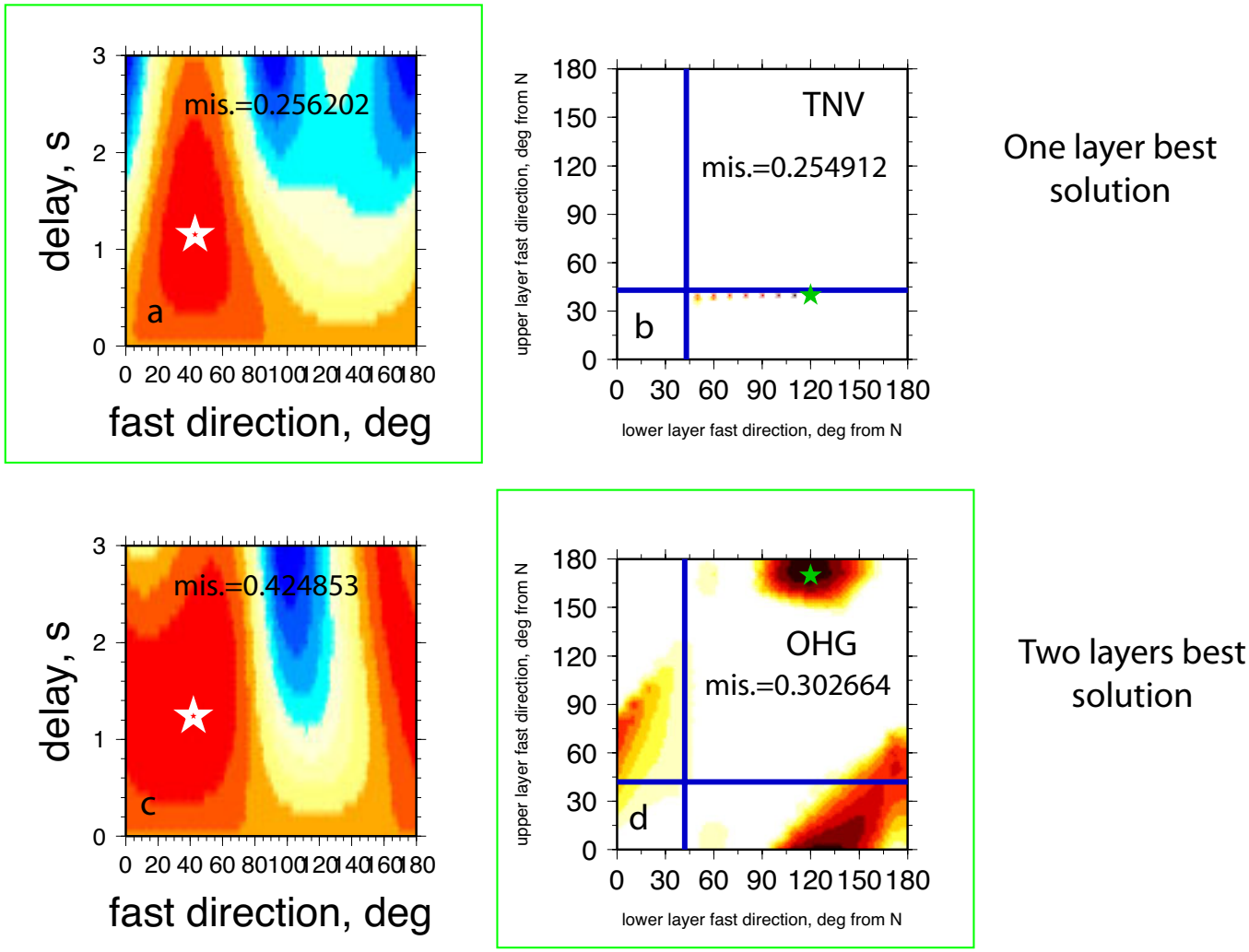

FIGURE S1: Examples of error surface plots calculated in the grouped inversion for TNV and OHG stations in one (a and c) and two layers (b and d) cases. a,c) The white star indicates the minimum misfit error model. b,d) In white all regions where errors are greater than the one layer estimator; coloured areas correspond to regions where errors are smaller for the two-layer case. The two blue crossing-lines correspond to the one layer model solution. Green star is the lowest error misfit model. The more complex model is chosen considering the distribution of the models on error surface plots and on the misfit reduction. For TNV therefore the one-layer model is chosen as the best fitting whereas the two-layer model seems to be the best for OHG.

TABLE S1: Coordinates of permanent and temporary stations operating in the Victoria Land region.

STATION	LAT. (˚)	LON. (˚)	ELEV. (m)
HUGH	-75,390	162,202	215
JYCE	-75,618	160,891	1230
MDAN	-75,799	161,798	780
MORR	-75,656	159,072	880
PRST	-75,224	161,909	475
PHIL	-75,219	162,545	425
TRIO	-75,491	159,687	1150
OHG	-75,136	161,137	630
STAR	-75,899	162,593	68
TNV	-74,700	164,120	40
VNDA	-77,517	161,853	151

TABLE S2: Table of single measurements obtained with Silver and Chan [1991] technique.

STATION	Event	BAZ (°)	Fast (°)	Delay (s.)	Quality
HUGH	06-Jan-2006	295,2	69,2	1,8	Good
HUGH	21-Jan-2006	293,5	-42,5	3,7	Good
HUGH	27-Nov-2005	261,4	37,4	2,3	Good
MDAN	25-Dec-2003	112,8	-49,2	0,6	Fair
MDAN	16-Jan-2004	159,2	19,2	2,1	Fair
MDAN	29-Dec-2003	345,6	33,6	3,2	Fair
OHG	10-Dec-2003	323,1	11,1	1	Good
OHG	27-Nov-2005	262,6	-23,4	1,7	Good
OHG	03-Dec-2005	332,2	30,2	2,5	Good
OHG	18-Jan-2006	343,7	-76,3	0,6	Good
PHIL	23-Dec-2005	119,4	5,4	2,0	Fair
PRST	30-Nov-2005	344,8	42,8	1,7	Fair
STAR	03-Feb-2005	291,4	-24,6	1,9	Good
STAR	05-Feb-2005	292,8	-3,2	1,7	Good
STAR	16-Feb-2005	292,6	72,6	2,0	Good
STAR	22-Feb-2005	80,9	-53,1	1,5	Good
STAR	22-Feb-2005	291,1	-12,9	1,8	Good
STAR	22-Feb-2005	337,5	-62,5	1,4	Good
STAR	24-Feb-2005	293,2	-10,8	3,4	Good
STAR	25-Feb-2005	292,7	60,7	0,9	Good
STAR	05-Mar-2005	322,4	12,4	2,0	Good
STAR	17-Mar-2005	101,9	-34,1	2,9	Good
STAR	04-Apr-2005	295,0	-29,0	1,7	Good
STAR	08-May-2005	83,1	-68,9	3,2	Good
STAR	30-Aug-2005	343,3	39,3	2,0	Good
STAR	20-Sep-2005	241,5	13,5	2,8	Good
STAR	17-Feb-2006	340,4	-77,6	2,6	Good
STAR	07-Mar-2006	274,5	36,5	3,4	Good
STAR	27-Mar-2006	333,0	-67,0	2,6	Good
STAR	01-Apr-2006	321,5	9,5	2,6	Good
STAR	14-Apr-2006	295,6	-20,4	1,0	Good
STAR	13-May-2006	292,5	-13,5	3,8	Good
STAR	12-Sep-2006	324,2	10,2	1,6	Good
STAR	05-Dec-2006	107,7	-40,3	1,0	Good
STAR	07-Mar-2007	322,5	-85,5	3,2	Good
STAR	13-Mar-2007	80,2	-53,8	1,3	Good
STAR	18-Mar-2007	344,3	-51,7	2,6	Good
STAR	06-May-2007	319,6	-82,4	1,7	Good
STAR	29-Aug-2007	321,5	-0,5	2,1	Good
STAR	03-Dec-2005	338,9	8,9	1,1	Good
STAR	05-Feb-2005	343,9	21,9	0,9	Fair
STAR	16-Mar-2005	346,9	40,9	2,3	Fair
STAR	09-May-2005	292,8	-1,2	2,3	Fair
STAR	13-Sep-2005	290,6	-39,4	2,9	Fair
STAR	19-Apr-2006	295,1	-4,9	2,1	Fair
STAR	12-Oct-2006	292,9	46,9	2,0	Fair
STAR	20-Oct-2006	320,2	78,2	2,4	Fair
STAR	24-Feb-2007	117,9	-20,1	0,8	Fair
STAR	25-Feb-2007	80,3	-49,7	1,0	Fair
STAR	20-Apr-2007	325,7	9,7	1,8	Fair
STAR	04-May-2007	182,6	28,6	3,0	Fair
STAR	07-May-2007	301,8	3,8	2,1	Fair
STAR	06-Sep-2007	322,8	12,8	2,2	Fair
TNV	21-Oct-2006	318,6	80,6	2,1	Good
TNV	20-Oct-2006	318,8	84,8	2,6	Good
TNV	03-Feb-2006	290,7	54,7	2,8	Good
TNV	01-Apr-2006	320,3	-85,7	1,0	Good
TNV	06-Aug-2006	341,7	15,7	2,4	Good
TNV	28-Jul-2006	321,7	25,7	2,1	Good
TNV	17-Feb-2006	180,8	40,8	2,4	Good
TNV	09-Mar-2006	169,4	-46,6	3,9	Good
TNV	04-Aug-2006	122,0	-16,0	0,8	Good
TNV	25-Sep-2006	331,4	-66,6	1,4	Good
TNV	10-Apr-2006	157,5	13,5	2,2	Good
TNV	14-Aug-2006	125,9	3,9	1,4	Good

TNV	14-Apr-2006	294,8	72,8	3,8	Good
TNV	15-Jan-2007	337,8	15,8	3,5	Good
TNV	30-Jan-2007	341,8	35,8	1,3	Good
TNV	25-Feb-2007	78,1	-71,9	2,2	Good
TNV	17-Mar-2007	115,4	-22,6	1,4	Good
TNV	18-Mar-2007	115,4	-30,6	3,6	Good
TNV	06-Jul-2007	97,1	53,1	1,6	Good
TNV	16-Jul-2007	334,8	22,8	0,6	Good
TNV	17-Jul-2007	232,6	-7,4	2,6	Good
TNV	21-Jul-2007	125,5	75,5	0,7	Good
TNV	29-Aug-2007	320,2	22,2	2,3	Good
TNV	29-Aug-2007	104,2	66,2	1,9	Good
TNV	01-Sep-2007	79,4	-62,6	1,5	Good
TNV	06-Sep-2007	321,4	-68,6	2,5	Good
TNV	28-Sep-2007	340,0	52,0	1,1	Good
TNV	30-Sep-2007	341,8	49,8	3,2	Good
TNV	06-Oct-2007	343,9	49,9	2,2	Good
TNV	25-Apr-2006	292,6	66,6	0,8	Fair
TNV	13-May-2006	291,0	61,0	1,7	Fair
TNV	21-May-2006	109,5	47,5	2,2	Fair
TNV	18-Oct-2006	111,3	-24,7	1,4	Fair
TNV	16-Apr-2006	337,2	-72,8	2,7	Fair
TNV	11-Jan-2007	346,0	-46,0	2,0	Fair
TNV	07-Mar-2007	163,3	7,3	0,8	Fair
TNV	09-Mar-2007	104,4	-57,6	2,6	Fair
TNV	30-Mar-2007	345,2	49,2	1,6	Fair
TNV	13-Jun-2007	101,2	67,2	1,4	Fair
TNV	12-Jul-2007	122,4	-79,6	3,8	Fair
TNV	16-Jul-2007	121,1	-6,9	3,6	Fair
TNV	06-Sep-2007	321,5	-64,5	2,2	Fair
TNV	10-Sep-2007	116,3	76,3	1,4	Fair
TRIO	26-Dec-2005	342,6	-57,4	2,9	Good
TRIO	30-Dec-2005	115,6	55,6	2,6	Good
TRIO	27-Nov-2005	263,8	33,8	1,9	Good
TRIO	25-Nov-2005	326,7	14,7	3,4	Fair
TRIO	31-Jan-2006	296,3	70,3	2,2	Fair
VNDA	04-Nov-2005	295,1	7,1	3,0	Good
VNDA	26-Dec-2004	325,2	-78,8	1,3	Good
VNDA	21-Aug-2005	94,9	-27,1	1,8	Good
VNDA	19-Dec-2004	322,3	36,3	3,6	Good
VNDA	18-Dec-2005	294,1	80,1	1,4	Good
VNDA	01-Jan-2005	293,8	-22,2	1,6	Good
VNDA	27-Dec-2004	293,8	-26,2	2,2	Good
VNDA	14-Jan-2005	292,2	42,2	3,6	Good
VNDA	26-Dec-2004	292,5	-21,5	1,2	Good
VNDA	28-Dec-2004	293,8	-88,2	3,2	Good
VNDA	09-Nov-2004	339,3	-72,7	1,4	Good
VNDA	09-May-2005	293,5	71,5	1,7	Good
VNDA	21-May-2005	293,5	71,5	3,2	Good
VNDA	31-May-2005	293,1	-18,9	0,6	Good
VNDA	03-Dec-2005	339,6	19,6	2,8	Good
VNDA	05-Jan-2005	293,2	77,2	1,0	Good
VNDA	02-Jan-2005	291,8	63,8	1,0	Good
VNDA	05-Aug-2004	345,0	29,0	2,3	Good
VNDA	28-Dec-2004	293,3	75,3	1,8	Good
VNDA	05-Feb-2005	293,3	-16,7	2,1	Good
VNDA	04-Jan-2005	292,2	80,2	1,2	Good
VNDA	06-Jan-2005	291,7	71,7	1,2	Good
VNDA	13-Aug-2005	344,8	-49,2	3,0	Good
VNDA	05-May-2005	114,2	-25,8	2,2	Good
VNDA	10-Feb-2005	113,9	-18,1	2,4	Good
VNDA	15-Nov-2004	119,1	65,1	0,6	Good
VNDA	25-Oct-2004	168,9	50,9	1,6	Good
VNDA	30-Dec-2004	292,7	-27,3	1,1	Fair
VNDA	31-Dec-2004	293,7	-6,3	0,6	Fair
VNDA	21-May-2005	117,2	55,2	0,6	Fair
VNDA	28-Jan-2005	116,3	52,3	1,2	Fair
VNDA	30-Jan-2005	116,7	82,7	1,4	Fair
VNDA	23-Dec-2005	120,3	86,3	0,4	Fair

VNDA	04-Jan-2005	291,6	-20,4	1,0	Fair
VNDA	23-Mar-2004	343,7	29,7	1,4	Fair
VNDA	28-Nov-2005	345,0	53,0	1,6	Fair
VNDA	24-Aug-2005	92,3	-27,7	2,9	Fair

Table S3: Table of null measurements obtained with Silver and Chan [1991] technique.

STATION	Event	BAZ (°)	Fast (°)	Delay (s.)	Quality
HUGH	27-Nov-2005	294,6	-55,4	2,7	Good
HUGH	21-Dec-2005	112,8	-7,2	3,6	Good
OHG	27-Nov-2005	262,6	-23,4	1,7	Good
OHG	31-Jan-2006	294,8	-45,2	4	Good
OHG	05-Dec-2005	228,4	-23,6	2,7	Fair
PRST	30-Nov-2005	344,8	42,8	1,7	Fair
PRST	18-Jan-2006	343,4	-2,6	4	Fair
PRST	18-Jan-2006	343	-41	3	Fair
PRST	02-Dec-2005	343	65	2,9	Fair
STAR	09-Feb-2005	342,9	54,9	3,6	Fair
STAR	16-Apr-2005	294,8	6,8	2	Fair
STAR	16-Aug-2005	342,3	48,3	3,2	Fair
STAR	30-Aug-2005	343,3	-86,7	2,4	Fair
STAR	06-Sep-2005	322,6	30,6	3	Fair
STAR	14-Feb-2006	344,6	56,6	3	Fair
STAR	01-Mar-2006	319,3	31,3	1	Fair
STAR	16-Sep-2006	292,8	4,8	1,9	Fair
STAR	29-Sep-2006	132,7	-25,3	2	Fair
STAR	07-Apr-2007	293,1	3,1	3,8	Fair
STAR	26-Sep-2007	118,3	-81,7	1,8	Fair
STAR	28-Sep-2007	341,4	53,4	4	Fair
STAR	15-Nov-2005	341,2	-34,8	3,2	Fair
STAR	14-Nov-2005	344,8	44,8	2	Fair
STAR	21-Apr-2007	322,0	26,0	4,0	Good
STAR	07-Apr-2005	288,6	0,6	2,5	Good
STAR	29-Sep-2006	132,9	-65,1	4	Good
STAR	18-Oct-2006	113	-57	2,7	Good
STAR	20-Apr-2007	328,8	-71,2	3,5	Good
TNV	06-Jan-2006	293,4	5,4	2	Good
TNV	05-Jun-2006	167,2	-54,8	3,4	Good
TNV	27-Jun-2006	97,3	17,3	4	Good
TNV	06-Apr-2006	273	15	2	Good
TNV	07-Mar-2006	273,6	53,6	2,9	Good
TNV	16-Jun-2006	342,7	62,7	1,5	Good
TNV	24-Feb-2007	116,4	38,4	2,9	Good
TNV	04-Apr-2007	340	80	1,8	Good
TNV	21-Apr-2007	320,8	-61,2	2,2	Good
TNV	06-May-2007	318,2	-49,8	3,6	Good
TNV	16-May-2007	300,7	12,7	3,6	Good
TNV	22-Aug-2007	340,5	60,5	3,1	Good
TNV	09-Aug-2007	319,8	85,8	4,0	Good
TNV	19-Aug-2007	338,5	40,5	4,0	Good
TNV	26-Sep-2007	116,8	22,8	4	Good
TNV	26-Apr-2006	292,3	10,3	3,3	Fair
TNV	12-Oct-2006	291,4	5,4	2,2	Fair
TNV	18-Jan-2006	341,4	33,4	2,4	Fair
TNV	28-May-2006	319,5	85,5	3,1	Fair
TNV	11-Aug-2006	89,7	-72,3	2,1	Fair
TNV	11-Mar-2007	346,7	-27,3	3,2	Fair
TNV	07-Apr-2007	291,6	37,6	3,8	Fair
TNV	18-Apr-2007	341,6	47,6	2,6	Fair
TNV	27-Apr-2007	291,2	-48,8	2,1	Fair
TNV	23-May-2007	93,1	27,1	2	Fair
TNV	16-Jul-2007	338	56	2,2	Fair
TNV	01-Aug-2007	335,9	-8,1	1,6	Fair
TNV	07-Aug-2007	326,2	-47,8	3,2	Fair
TNV	30-Sep-2007	341,8	-80,2	3,2	Fair
VNDA	10-Dec-2004	340,3	46,3	2,1	Fair
VNDA	17-Feb-2005	293,7	53,7	1,9	Fair
VNDA	04-May-2005	342,3	-41,7	3	Fair
VNDA	31-Dec-2004	291,9	37,9	3	Fair
VNDA	07-Apr-2005	295,2	-32,8	2,7	Good

VNDA	31-Mar-2005	295,1	45,1	1,1	Good
VNDA	03-Apr-2005	295,9	-30,1	0,9	Good
VNDA	09-Feb-2005	293,7	33,7	2,6	Good
VNDA	09-Jan-2005	293,7	29,7	3,2	Good
VNDA	02-Feb-2005	343,4	67,4	2,9	Good
VNDA	31-Dec-2004	291,7	-52,3	4	Good
VNDA	05-May-2005	113,6	37,6	2,9	Good
VNDA	06-Aug-2004	295,1	-14,9	4,0	Good

Table S4: Table of averaged single measurements.
Quality indicates if the mean is calculated using good and fair or only fair measurements.

STATION	Φ (˚)	dt (s.)	Quality
STAR	-8,2	2,1	good
TNV	59,2	2,1	good
VNDA	50,5	1,8	good
OHG	1,4	1,5	good
HUGH	61,1	2,6	good
TRIO	49,1	2,6	good
PHIL	5,4	2,0	fair
PRST	42,8	1,7	fair
MDAN	14,2	2,0	fair

Table S5: Results of grouped inversion. The 10 best models in one and two layer's cases are listed for any stations

1-Layer Models

STAZ	fast (°)	dt (s)	misfit
TNV	43	1,2	0.256202
TNV	42	1,2	0.256211
TNV	43	1,2	0.256224
TNV	42	1,2	0.256232
TNV	44	1,2	0.256608
TNV	41	1,2	0.256639
TNV	44	1,2	0.256646
TNV	43	1,1	0.256671
TNV	41	1,2	0.256673
TNV	42	1,1	0.256685
VNDA	38	1,0	0.258683
VNDA	37	1,0	0.258706
VNDA	37	1,1	0.258795
VNDA	38	1,0	0.258806
VNDA	38	1,1	0.258856
VNDA	37	1,0	0.258912
VNDA	39	1,0	0.259017
VNDA	39	1,0	0.259039
VNDA	36	1,0	0.259099
VNDA	36	1,1	0.259123

2-Layer Models

STAZ.	fast -lower (°)	dt -lower (s)	fast -upper (°)	dt -upper (s)	misf .
OHG	120	1,2	-10	2,9	0.302664
OHG	130	1,3	0	2,4	0.311183
OHG	120	1,3	0	2,7	0.312411
OHG	130	1,2	-10	2,6	0.312452
OHG	140	1,3	0	2,1	0.317195
OHG	140	1,4	10	2,0	0.322043
OHG	150	1,5	10	1,7	0.326347
OHG	130	1,4	10	2,4	0.327979
OHG	150	1,6	20	1,7	0.330305
OHG	140	1,3	-10	2,4	0.330961
STAR	150	2,3	40	1,2	0.288839
STAR	140	1,4	10	1,1	0.289274
STAR	150	1,9	30	0,9	0.289294
STAR	130	1,1	0	1,4	0.289368
STAR	110	1,0	-10	1,9	0.290709
STAR	100	1,2	-10	2,2	0.291630
STAR	140	1,7	20	1,2	0.291950
STAR	120	1,2	0	1,6	0.292482
STAR	120	0,9	-10	1,6	0.295421
STAR	130	1,4	10	1,4	0.295840